AEROSPACE REPORT NO.
ATR-2021-02026

Relativistic Proton Spectrometer Electron Response

September 27, 2021

M. D. Looper[1], T. P. O'Brien[1], and J. E. Mazur[2]
[1]Space Sciences Department, Space Science Applications Laboratory
[2]Space Science Applications Laboratory, Physical Sciences Laboratories

Prepared for:

JHU/APL
11100 Johns Hopkins Road
Laurel, MD 20723-6099

Contract No. 135557

Authorized by: Engineering and Technology Group

Acknowledgments

The authors acknowledge many useful discussions with members of the Space Science Applications Laboratory and xLAB, as well as members of the Van Allen Probes team.

Abstract

Two identical Relativistic Proton Spectrometer (RPS) sensors were launched in 2012 aboard NASA's twin Van Allen Probes to measure protons from about 60 MeV to >1 GeV. In addition, however, these sensors were predicted, and were found in flight, to respond to geomagnetically trapped electrons above several MeV. This document describes this response, showing how outer-zone electrons can be distinguished from the protons that dominate the sensors' measurements. We also show how the sensors detected a population of extremely high energy (tens of MeV) electrons at low L, whose origin is currently under investigation. The data shown herein are calibrated as described in a companion report [2]; these two reports are intended as supplements to a third report [4] that describes how RPS data were used to derive the energy and angular distributions of the protons that the sensors were flown to measure.

Contents

Figures

1. Sensor Configuration

Two identical Relativistic Proton Spectrometer units, referred to hereinafter as RPS-A and RPS-B, were launched into a near-equatorial geostationary transfer orbit (GTO) aboard the two Van Allen Probes A and B (formerly Radiation Belt Storm Probes). The sensors, their mission, and ground calibrations performed before launch were described by Mazur et al. [3]. The detector complement of each RPS unit comprised a Solid State Detector Assembly (SSDA) with twelve circular silicon detectors and a Cherenkov Radiator Assembly (CRA) with a magnesium fluoride radiator whose light was collected by a microchannel-plate (MCP) photomultiplier "tube" (PMT).

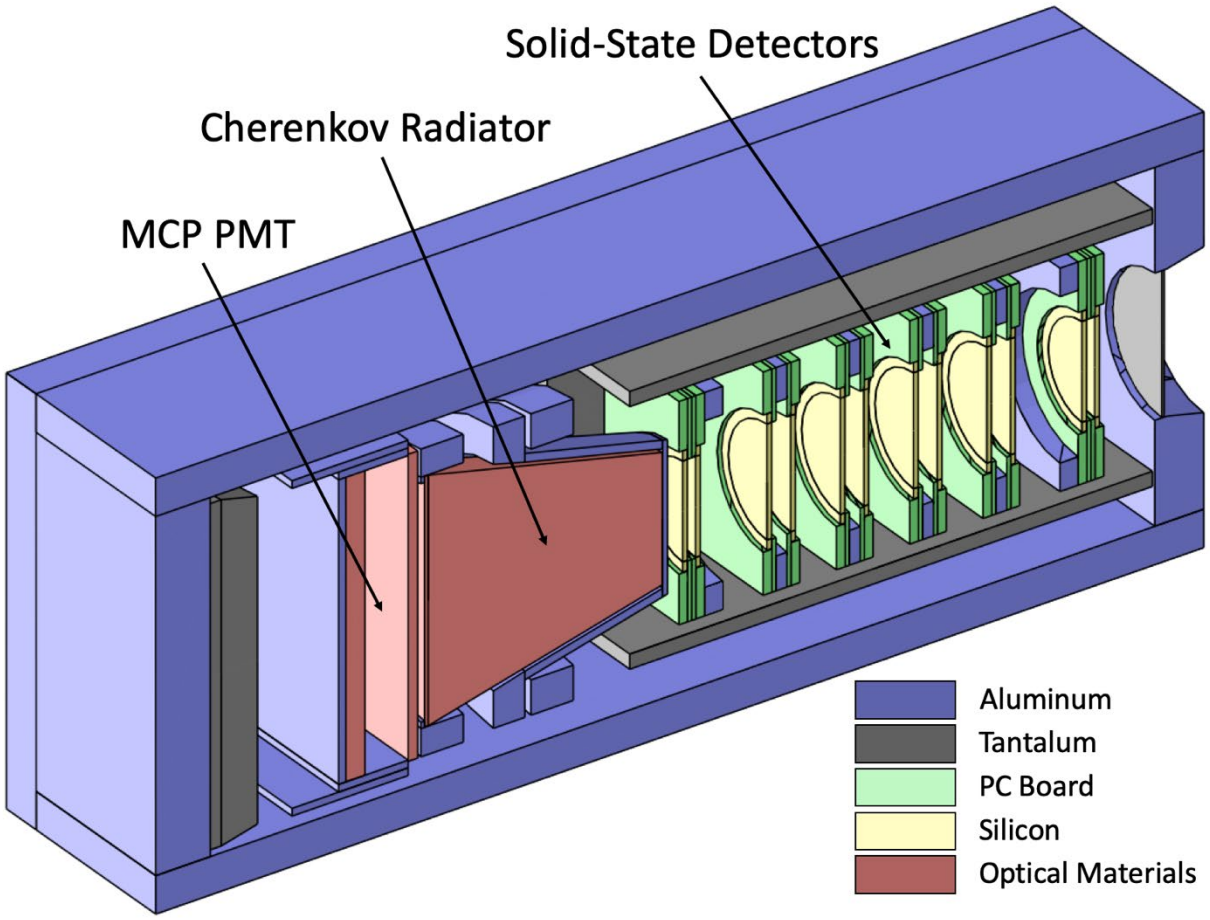

Figure 1. Diagram of RPS active elements and the inert material around them, as simulated with Geant4. Colors identify materials as shown in the legend and discussed in the main text.

Figure 1 is a diagram of the active elements of RPS and of the inert material around them. The instrument was designed to measure protons coming in through the (gray) 20-mil-thick tantalum window at extreme right. The detectors of the SSDA, all of which are 1 mm thick, are lined up behind this window, with particles passing first through two detectors with active areas 20 mm in diameter, A1 and A2. The next eight detectors, numbered D1 through D8 from the one nearest the aperture, have active areas 23 mm in diameter, and the last two are smaller 20-mm detectors again, A3 and A4. Only the eight D detectors were pulse-height analyzed, with their energy deposits being recorded in direct events that were sent to Earth in the telemetry; the A detectors were used only to define an acceptance cone. For an event to be recorded,

the discriminators of a pair of aperture detectors, nominally A1 and A3 (with A2 and A4 as a backup that was never used during the mission), needed to be triggered, along with those of all eight D detectors in between; each detector's discriminator was nominally triggered by 0.2 MeV of energy deposit. The D detectors are larger so that particles traveling in a straight line between the two aperture detectors required by the coincidence conditions would not pass near the outer edges of the active areas of the D detectors. This ensures that the energy deposits in the D detectors that were determined by pulse-height analysis of their output would not be underreported due to edge effects.

Behind the SSDA is the magnesium fluoride crystal radiator of the CRA. This was shaped so that the Cherenkov light of relativistic particles coming through the aperture and SSDA would be funneled by total internal reflection to the faceplate of the microchannel plate photomultiplier immediately behind the radiator. The paths of Cherenkov photons generated by relativistic particles going backward through the stack, by contrast, would strike the conical wall of the radiator at angles that would allow many of them to escape and thus not be counted by the PMT. In addition, the small end of the radiator cone was painted black, to further reduce the collection of Cherenkov light from any backward-going particles. The optically active materials in the sensor, comprising the MgF_2 radiator, the fused-quartz faceplate of the PMT, and the microchannel plate behind it, are shown in red. Finally, at the left end of the stack is a tantalum absorber 1 cm thick, to reduce background from penetrating particles going backward through the stack.

2. Simulated Detector Response

The diagram in Figure 1 was generated by Geant4, an open-source Monte Carlo radiation-transport toolkit [1], and represents the geometric model used in the simulations of the RPS response presented below. The tenfold detector coincidence that was required in order for a particle event to be analyzed (elevenfold if the CRA recorded a signal) resulted in response that was very strongly collimated into a double-ended cone defined by the two aperture detectors (A1 and A3), with very little response to particles coming in from the sides. Thus, for the simulations reported herein we did not model in detail the shielding provided by the electronics box around the sensor or by the spacecraft itself, reducing them to an enclosing aluminum box 300 to 450 mils thick to represent the minimum shielding on each side of the detector stack.

In the remainder of this section, we will show the simulated response of SSDA and CRA to protons and electrons going both forward and backward through the detector stack, and then will show simulated observations of the combined SSDA and CRA output for a realistic incident proton spectrum. In the next section, we will compare these simulated observations with the real observations, showing where and how electrons can be distinguished from protons in the data. Details of how we iteratively determined the calibrations of individual detectors' pulse heights, including gain drifts with time and temperature, are given by Looper et al. [2]; the data presented in the next section all use the final calibrations detailed therein.

2.1 Solid-State Detectors

As discussed by Looper et al. [2], when we need to represent the eight SSDA pulse heights by a single number for plots, cuts, etc., we use the average of the two smallest of those pulse heights for a given event rather than the average of all eight pulse heights for that event. This algorithm, suggested by the late Norm Katz, rejects randomly-occurring large pulse heights in one or more detectors due to secondary particles, and tightens up the distribution of SSDA amplitudes for such analyses.

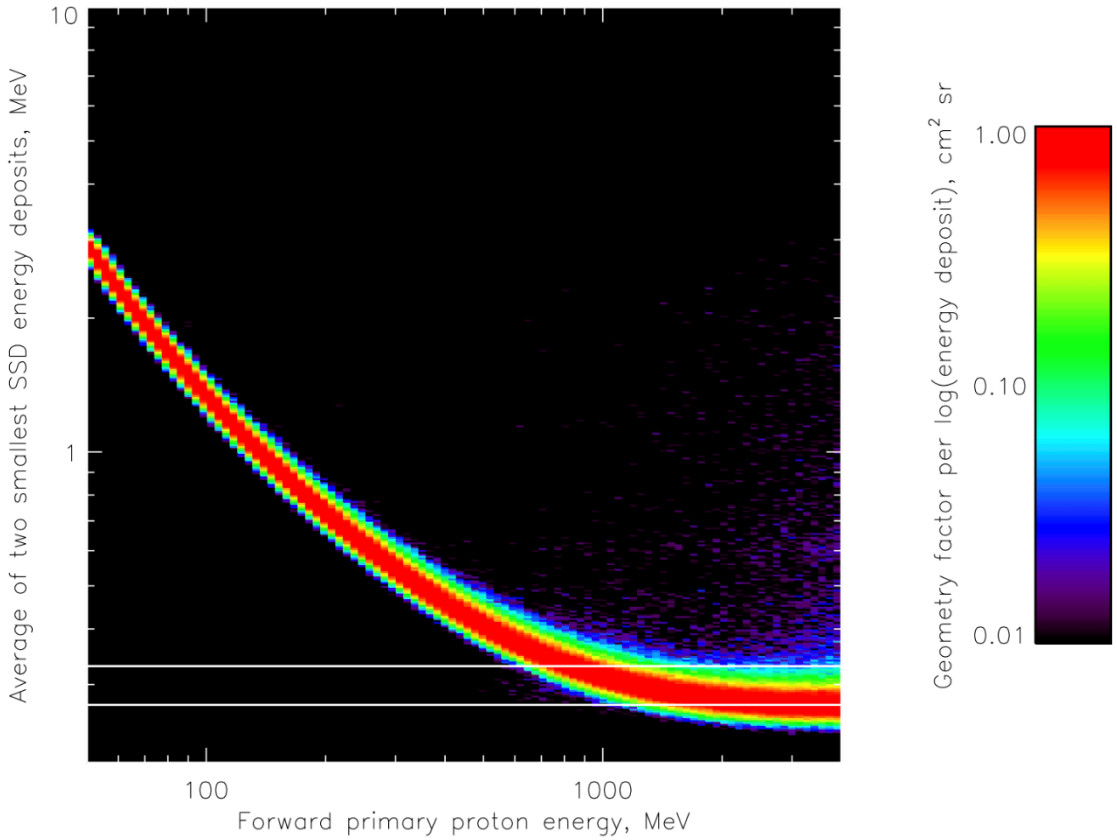

Figure 2. Distribution of the average of the two lowest simulated energy deposits in D1 through D8 for each event as a function of the incident energy of protons reaching the sensor from the hemisphere centered on the direction of a particle entering the aperture parallel to the axis of the detector stack. Colorscale is effective geometry factor for events falling in each energy-deposit bin, normalized to the logarithmic width of the bin. Horizontal white lines define a cut that will be referred to in section 2.2.

Figure 2 shows the distribution of this "minimum-two" value as a function of the incident energy of simulated protons distributed isotropically over the forward hemisphere, i.e., the half of the 4π sr of possible incidence directions that have a positive projection along the vector going straight into the aperture at the right of Figure 1. The minimum-two SSDA values cover a wide and continuous dynamic range, with the largest values being seen for protons that just penetrate the stack around 50 MeV primary proton energy and the smallest values at a broad minimum where relativistic particles lose the least energy due to ionization in the silicon detectors. The two horizontal white lines define a cut that will be referred to in section 2.2. A plot of response for backward-going protons (Figure 4 of [2], not shown here) looks similar, but with a higher threshold (about 200 MeV) due to the greater amount of mass that must be penetrated to enter the SSDA from the direction opposite the aperture.

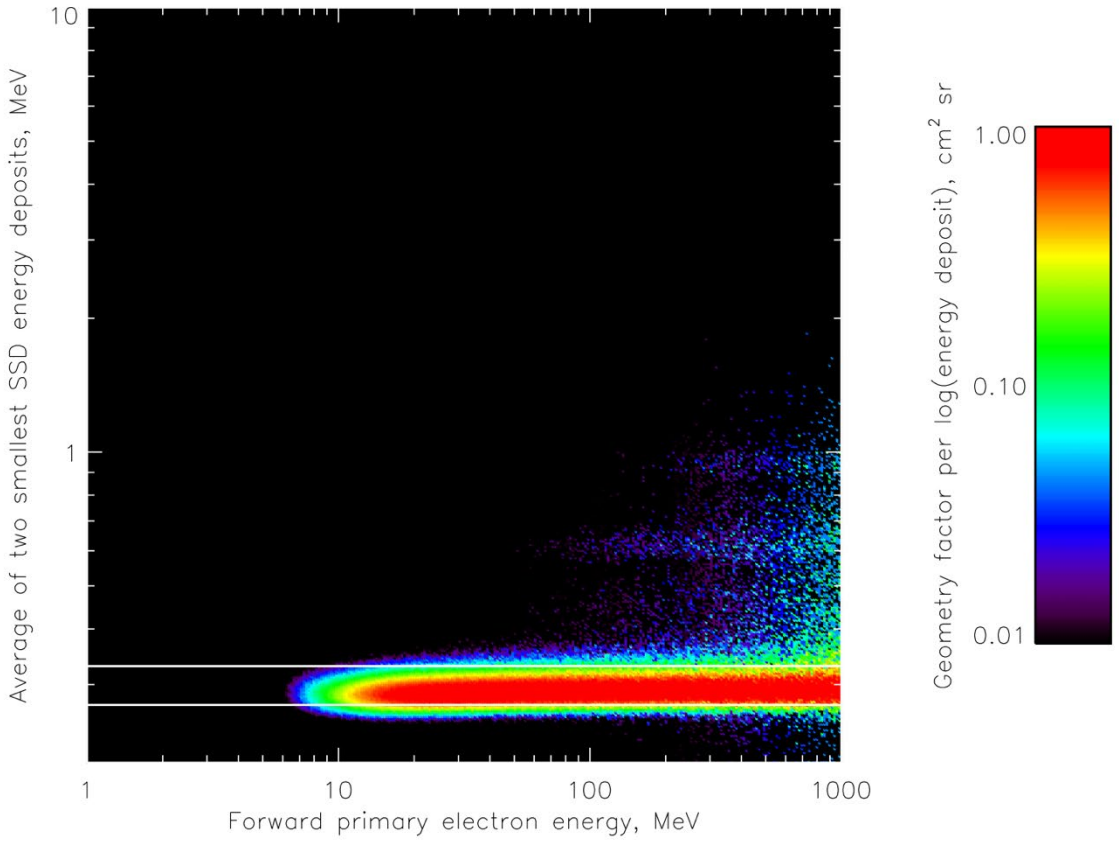

Figure 3. Distribution of the average of the two lowest simulated energy deposits in D1 through D8 for each event as a function of the incident energy of electrons reaching the sensor from the forward direction, as for protons in Figure 2. Colorscale is the same as in Figure 2, as are the horizontal white lines defining a cut to be used in section 2.2.

Figure 3 shows the distribution of minimum-two SSDA energy deposits for simulated electrons distributed isotropically over the forward hemisphere, as for protons in Figure 2. Because electrons must have very high energy to penetrate the window and the entire SSDA stack, essentially all of them deposit the energy that is characteristic of singly-ionized, relativistic "minimum-ionizing particles" (MIPs), which is around 0.3 MeV in these 1-mm-thick detectors. In some events one or two secondary electrons travel through the stack alongside the primary electron, depositing their own minimum-ionizing energy, so that there are sparse horizontal clusters of events at 0.6 and 0.9 MeV energy deposit above the main band (an even fainter horizontal band at 0.6 MeV, for a pair of secondary electrons traversing the stack after generation by a proton that just missed going through it, is visible in Figure 2.). As is the case for protons, the response for electrons over the backward hemisphere looks similar to this, but with a higher threshold (about 20 MeV).

2.2 Cherenkov Subsystem

Unlike most solid-state detector telescopes flown in space, RPS has a Cherenkov radiator to extend energy resolution and directional discrimination to higher energies than are possible with a detector stack like SSDA alone. A proton of a given energy will produce the same amount of Cherenkov light regardless of which direction it goes through the radiator crystal; however, as described in section 1, the CRA was designed to enhance collection of light from forward-going protons and to suppress collection of light from those traveling backwards through the radiator and the SSDA stack.

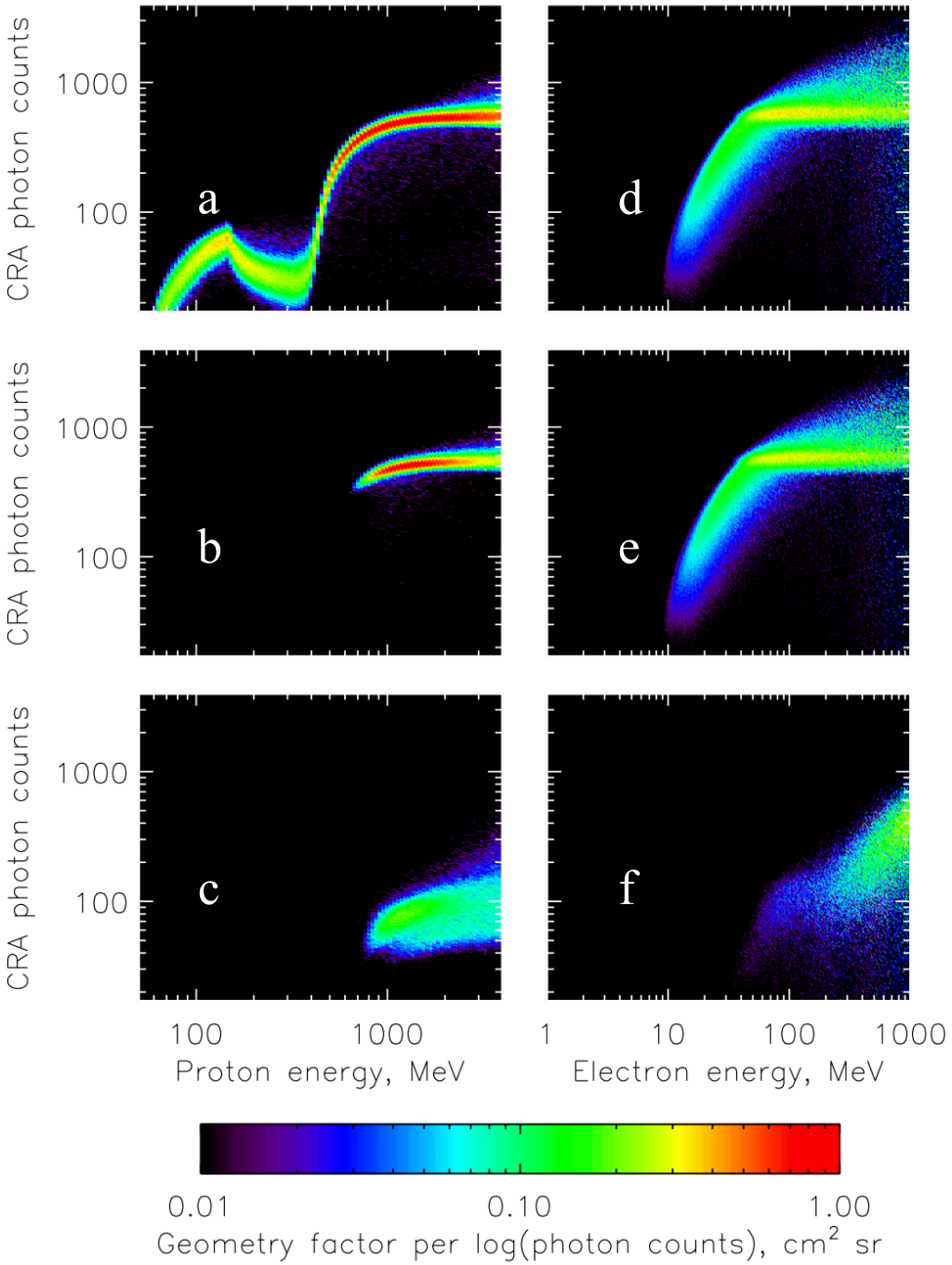

Figure 4. Distribution of number of photons counted by CRA as a function of the energy of simulated protons or electrons, with subpanels as discussed in the main text. Colorscale is effective geometry factor for events falling in each Cherenkov-count bin, normalized to the logarithmic width of the bin.

Figure 4 shows the number of photons counted by the simulated CRA for different subsets of electrons and protons, with six panels (4a to 4f) discussed in turn below. All panels share the colorscale at the bottom of the figure. Figure 4a shows the response of the simulated CRA for protons arriving over the forward hemisphere as in Figures 2 and 3. As in those figures, the colorscale is the geometric factor for events with a given primary proton energy that fall in each (in this case) photon-count bin, differential in the logarithm of the number of counts. This figure is a copy of Figure 5 of [2], and the contributions to the

complicated shape of the main band of response are discussed in detail there. Of greatest interest here, for comparison with the response of the sensor to electrons, is the highest-energy portion of the curve, where the Cherenkov response saturates at 500-600 photons per event. Such particles emit the maximum number of photons per unit pathlength as the proton's velocity approaches the speed of light in a vacuum, and that photon production is summed over the full length of the radiator crystal for these penetrating particles.

Figure 4b shows the distribution of CRA photon counts for these high-energy protons, selecting events with minimum-two SSDA energy deposits between 0.27 and 0.33 MeV, which are the values indicated by the horizontal white lines in Figure 2. The CRA response is now confined to the saturated band, with several hundred photon counts.

As discussed in section 1, the Cherenkov radiator is shaped so as to suppress the counting of Cherenkov photons from particles going backwards through the stack. A plot of the response of CRA to protons incident over the backward-going hemisphere, to complement Figure 4a for forward protons (Figure 6 of [2], not reproduced here) would have a structure similar to that of Figure 4a, but with lower numbers of photons counted; restricting consideration to backward protons with minimum-two SSDA energy deposits between 0.27 and 0.33 MeV, as in Figure 4b for forward protons, gives the distribution in Figure 4c. The distribution is wider vertically than that for forward protons in Figure 4b, but it is likewise confined to energies where the (backward) Cherenkov light output saturates.

Turning to the electrons, Figure 4d shows the distribution of CRA photon counts as a function of energy for electrons incident over the forward hemisphere. In common with the forward protons in Figure 4a, we see a rise in Cherenkov photons with energy from a threshold to a saturation level where electrons travel near the speed of light in vacuum through the full length of the crystal and thus radiate the maximum number of photons. Unlike in Figure 4a, we see a strong "supersaturation" above the horizontal saturated band at 500-600 photon counts: electrons produce more high-energy secondary electrons than do protons, and these secondary electrons emit their own Cherenkov light, adding to the total.

Figure 4e shows the distribution of Cherenkov photon counts for forward electrons that have minimum-two SSDA energy deposit between the cut values of 0.27 and 0.33 MeV. Because, as shown in Figure 3, the vast majority of the electrons that trigger the aperture detectors in SSDA deposit the minimum-ionizing amount of energy, applying this cut makes very little difference to the distributions between Figures 4d and 4e.

The same is true for electrons incident over the backward hemisphere: a plot of all such events' CRA response (not shown) is minimally different from Figure 4f, which shows the distribution of CRA photon counts for backward electrons with minimum-two SSDA energy deposits between 0.27 and 0.33 MeV. There is some weak response starting at 20-30 MeV, but we see the number of photons counted per event approach the (forward) saturation level of 500-600 counts only for the very highest energies, near a GeV. Thus, as for protons (comparing Figures 4b and 4c), we can see that for very high-energy electrons the Cherenkov radiator shape and orientation performs as designed, allowing us to distinguish backward- and forward-going particles where the task would be impossible with only an energy-deposit detector array like SSDA.

2.3 Combined Response

Of course, in the flight data we cannot directly sort out observable properties of measured particle events by the energy or direction of the protons causing them, as in Figures 2 through 4; rather, we see the aggregate of the observables for each event and try to deduce from them the properties of the causative particles. To simulate the observations, we need to assume a set of properties for those particles and then fold them through calculations like those above. For the simulation figure below, we modeled an

environment consisting of isotropic protons, and we assumed an energy spectrum based on an estimate of the daily average that was made early in the mission.

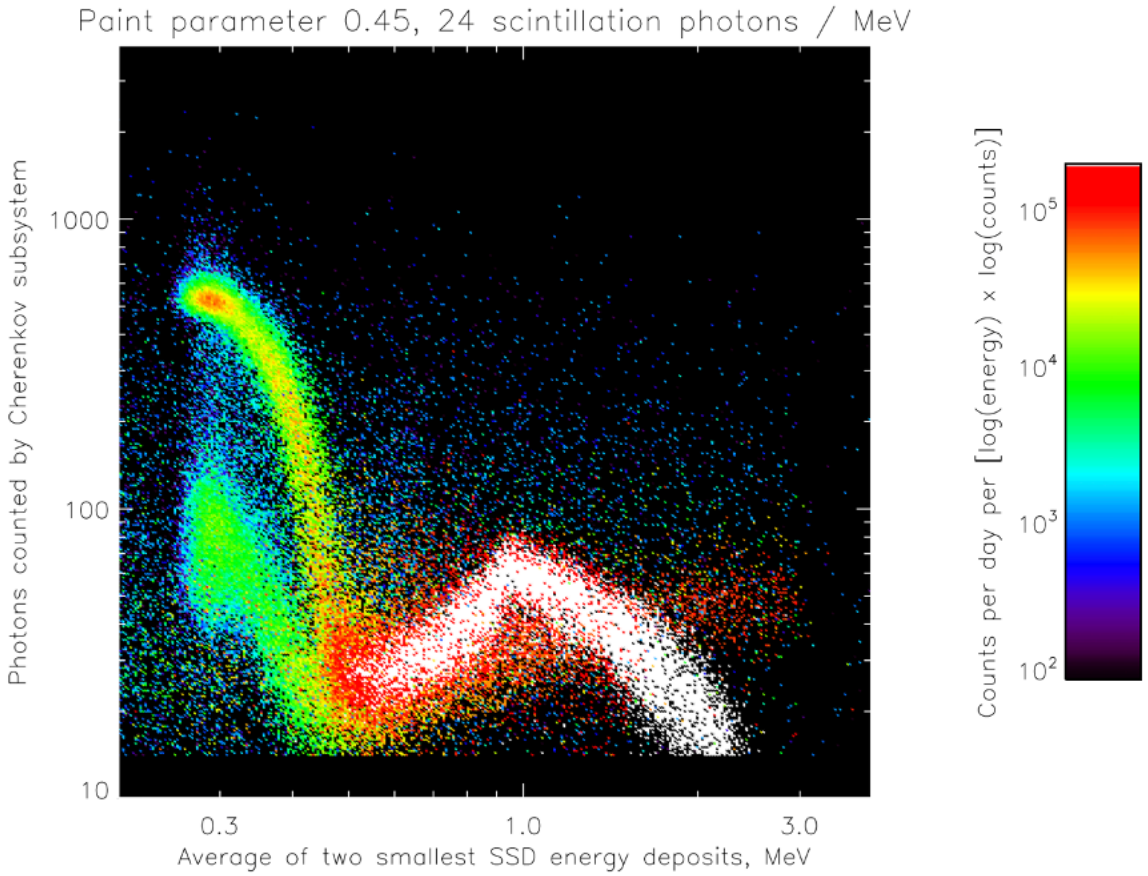

Figure 5. Distribution of Cherenkov count in CRA vs. minimum-two energy deposit in SSDA, for simulated events due to isotropic protons with a spectrum approximating the daily average early in the mission. The colorscale displays rate per bin, differential in the logarithm of energy deposit and the logarithm of photon counts.

Figure 5 shows the result of such a convolution, plotting the expected distribution of photon counts vs. the minimum-two energy deposit in SSDA. This is a copy of Figure 15 of [2], and its components are discussed further therein. (The plot label gives the values of two adjustable parameters in the simulations that we selected to get the best match to the distribution of events in the observations, also as discussed by Looper et al. [2].) Since, as seen in Figure 3, the vast majority of the electrons will have a minimum-two SSDA energy deposit clustered around the MIP value, we would expect that adding electrons to this simulation would add events in a vertical band around this value, and the relative intensity up and down that band representing greater or lesser amounts of Cherenkov light would give us at least some information about the energy distribution of those electrons, by way of the model results shown in Figure 4e.

3. Observations

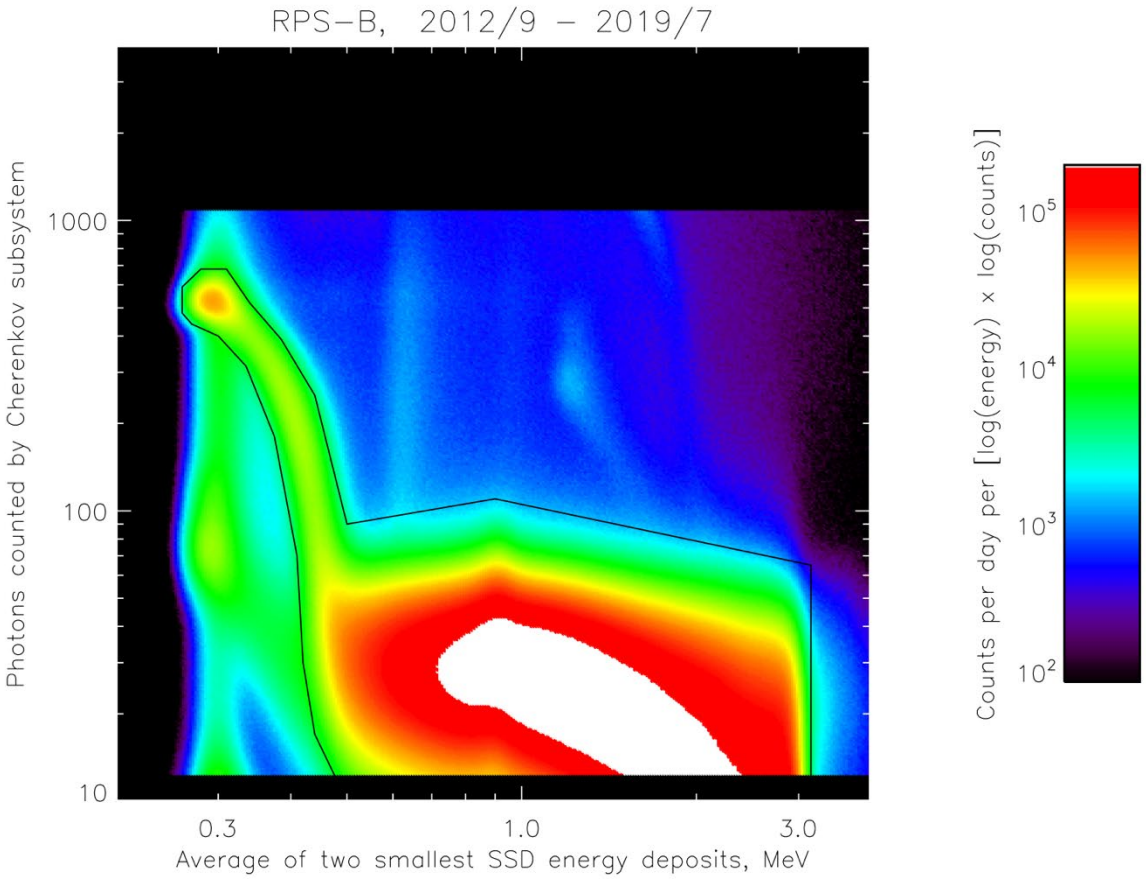

Figure 6. Distribution of Cherenkov count in CRA vs. minimum-two energy deposit in SSDA, for all RPS-B data during the mission. Black line indicates the cut that was used to separate forward protons from backward protons and other background events.

The distribution of CRA vs. SSDA measurements for RPS-B events collected during periods without energetic solar particle activity is shown in Figure 6, with the same colorscale as Figure 5. Early in the mission we started calling this sort of figure a "Nessie" plot because of the resemblance of the distribution of forward proton events, enclosed by the black line (as discussed by Looper et al. [2]), to a "head" due to relativistic protons atop a long "neck" due to lower-energy protons and attached to a "body" caused by protons whose CRA signal was dominated by scintillation rather than Cherenkov light. As in Figure 5, the backward protons are visible as a head and neck below those due to forward protons. The differences between the simulations in Figure 5 and the data in Figure 6, as well as the identification of other features of Figure 6 not mentioned hereinafter, are discussed by Looper et al. [2]. RPS-A observations look similar to those of RPS-B in Figure 6, but since that sensor's CRA had lower gain there were fewer channels of data at low photon counts, which as we will see in the next subsection is one place where electrons appear in the data. Thus, we will focus on RPS-B data in the rest of this report.

3.1 Outer-Zone Electrons

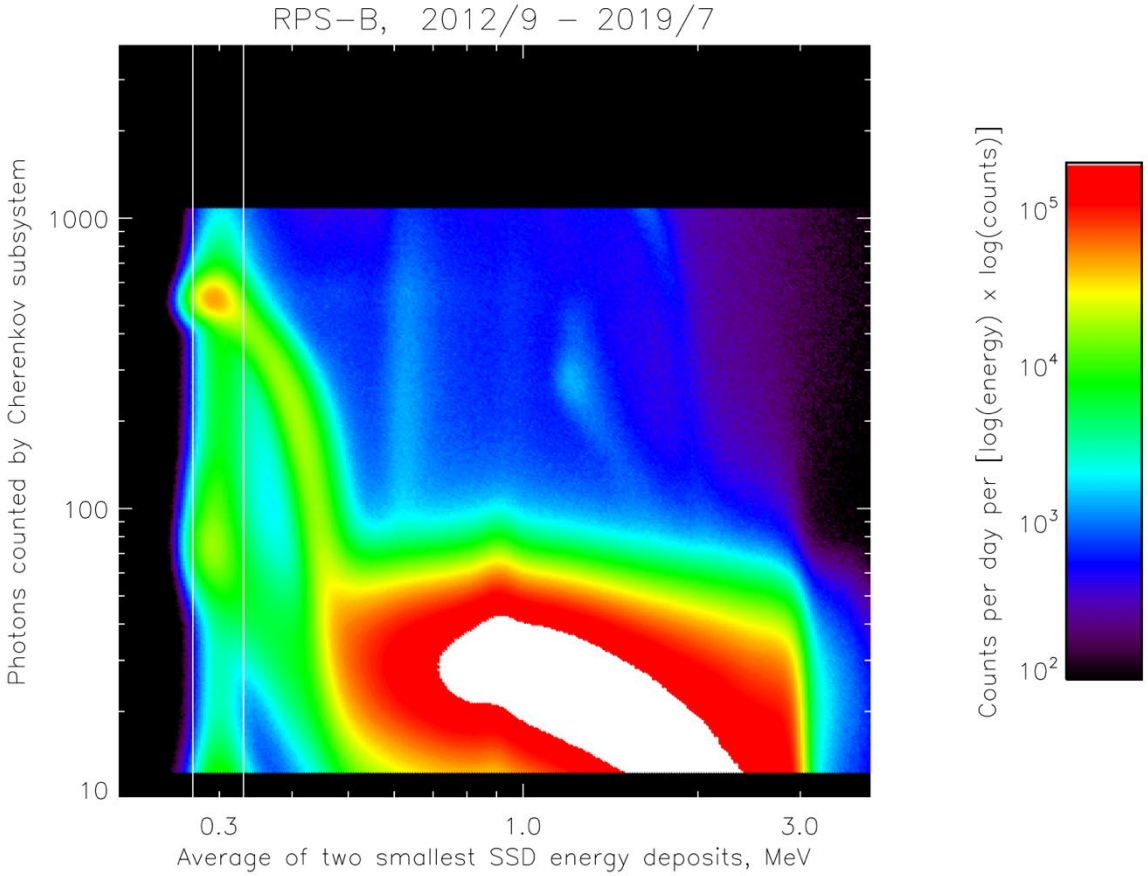

Figure 7. Distribution of Cherenkov count in CRA vs. minimum-two energy deposit in SSDA, for all RPS-B data during the mission, replicating Figure 6. White lines show the cut in minimum-two SSDA energy deposit as discussed in the text.

The white lines in Figure 3 show that the minimum-two SSDA energy deposits for electrons nearly all fall between 0.27 and 0.33 MeV. Figure 7 replicates the Nessie plot in Figure 6, but shows these two values as vertical white lines; we expect to find nearly all electron response in that region, mixing with the forward and backward proton heads. (The SSDA proton response in Figure 2 drops below 0.27 MeV for the highest energies, but few of these particles are present even among the galactic cosmic rays (GCRs), so the simulation results in Figure 5 and the observations in Figures 6 and 7 do not include many proton events to the left of the leftmost white line.)

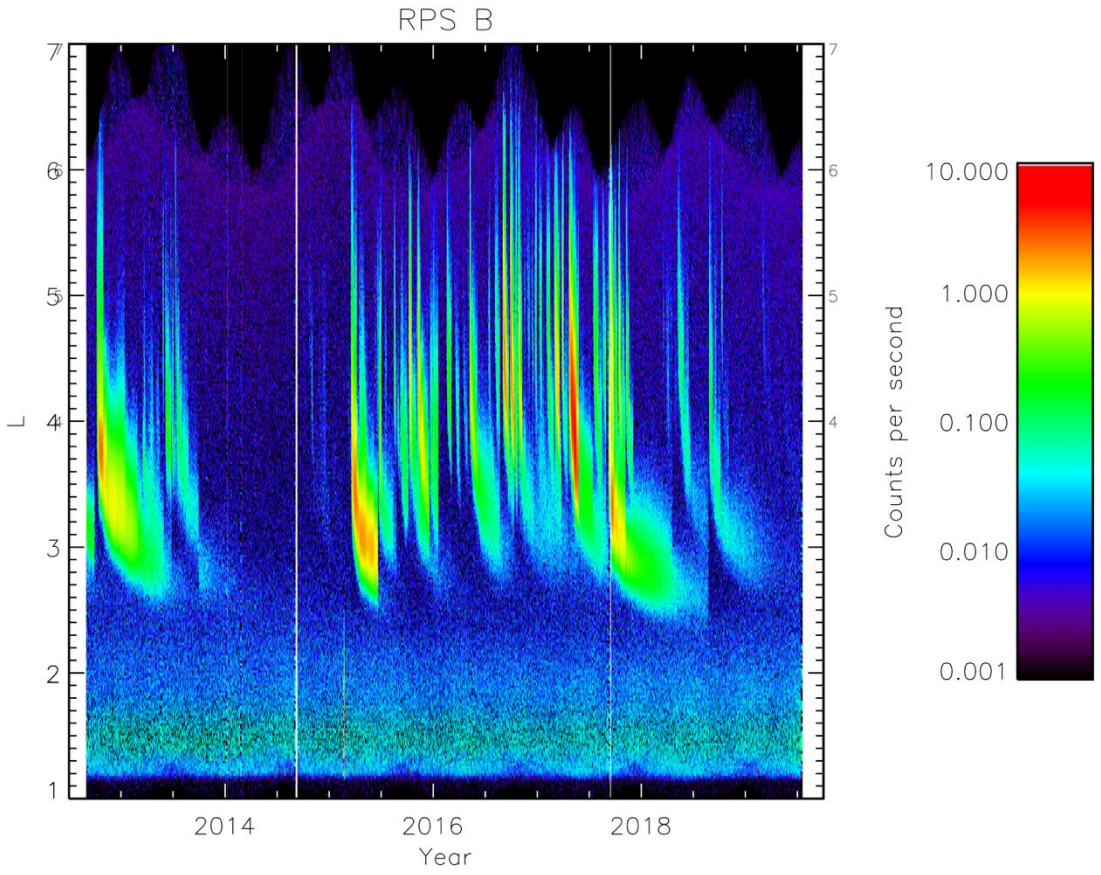

Figure 8. Time history of RPS-B outer-zone electron observations over the entire mission, as daily averages sorted by L.

The concentration within this SSDA band at the lowest values of CRA signal in Figures 6 and 7 is not present in the proton simulations of Figure 5, so electrons are naturally suspected as the cause. Figure 8 shows a time series of daily averaged countrates sorted by L in this region: minimum-two SSDA energy deposit is between 0.27 and 0.33 MeV, and CRA amplitude is 23 photons or less (including zero, for events where CRA gave no signal). The time series looks very much as would be expected for outer-zone electrons (with some inner-zone proton contamination still present at very low L); based on the simulation results in Figures 3 and 8, the RPS response in this band starts around 7-8 MeV and would include some response to any electrons present that have energies as high as 15-20 MeV. This population is well outside the black line defining the cut in Figure 6 that we used to select forward proton events for spectral analysis, so they do not contaminate this primary data product.

3.2 Extremely High Energy Electrons in the Inner Zone

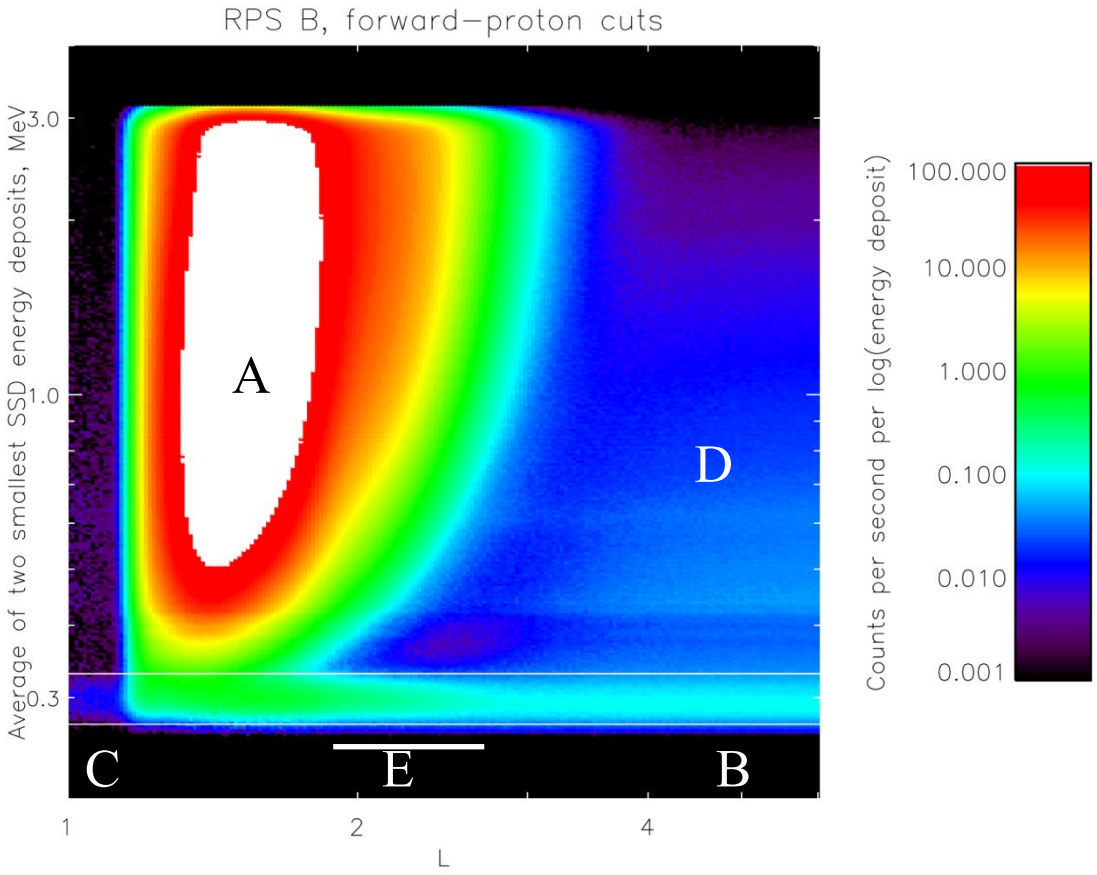

Figure 9. Distribution vs. L and minimum-two SSDA energy deposit of particle events recorded by RPS-B throughout its lifetime that fall inside the polygon cut for forward protons in Figure 6.

From prelaunch simulations, we had expected RPS to detect electrons in the outer zone as in Figure 8, with signals that stand apart from the proton contribution shown in Figures 5 to 7 so that they can readily be separated from the galactic cosmic ray (GCR) protons also present through the outer zone. However, in the course of analyzing the proton observations in the inner zone, we identified a subset of events around L = 2 that we have concluded consists instead of an unexpected population of extremely high energy electrons (30 MeV and up). Unlike the outer-zone electron events discussed in the previous subsection, the locations of these events in Figures 6 and 7 overlap to some extent the distribution of valid forward proton events, and so separation is more difficult. However, as described in the remainder of this section, there are differences that we can exploit to identify them and begin to localize and quantify them.

Figure 9 shows the distribution vs. L and minimum-two SSDA energy deposit of all events collected by RPS-B that fall inside the black line in Figure 6, which are thus identified as forward protons. The most intense region of the plot, labeled A, encompasses the geomagnetically trapped inner-zone protons, showing an upper limit in L that moves to lower values with declining energy deposit. Since energy deposit in turn declines with increasing energy, this reflects the fact that the outer boundary of the inner zone is set by the trapping limit, the distance from Earth at which the magnetic field becomes too weak to hold onto the protons. Because it takes a stronger field to trap higher-energy protons, their outer boundary is at a lower L than that of lower-energy protons.

GCRs are most prominently visible in the band above the label B, which is delimited by the MIP energy-deposit range shown as two horizontal white lines (0.27 to 0.33 MeV, as on Figures 2, 3, and 7). This band is present at a constant level throughout the outer zone above L = 3, but will decline toward lower L as the strengthening magnetic field deflects an increasing fraction of the GCR protons, leaving only a weak flux of the highest-energy GCRs visible above label C at L values below the lower limit of the trapped protons. (The energy deposits of lower-energy forward GCRs, in the region labeled D, are mixed with those of higher-energy GCRs going backward through the sensor as in Figure 5 and as discussed by Looper et al. [2]. These will not be discussed further herein.)

The population within the MIP band above label E, in approximately the L range shown by the heavy white horizontal line, has some characteristics that are distinctly different from those of the proton populations. As noted, the contribution to the MIP band of GCR protons is expected to decline toward lower L, but in this L range the MIP band intensifies toward lower L instead. As seen by the trapping-limit cutoff of the trapped protons at higher energy deposits, this L range is too high for protons energetic enough to fall into the MIP band to be trapped: it is not clear exactly where in L the trapping limit for MIP protons in the inner zone falls in this plot, but since protons just above 0.33 MeV energy deposit are outside the trapping limit in the range of L above the heavy white line, the MIP protons must be as well, so that we should only see untrapped GCR protons here declining in intensity toward lower L.

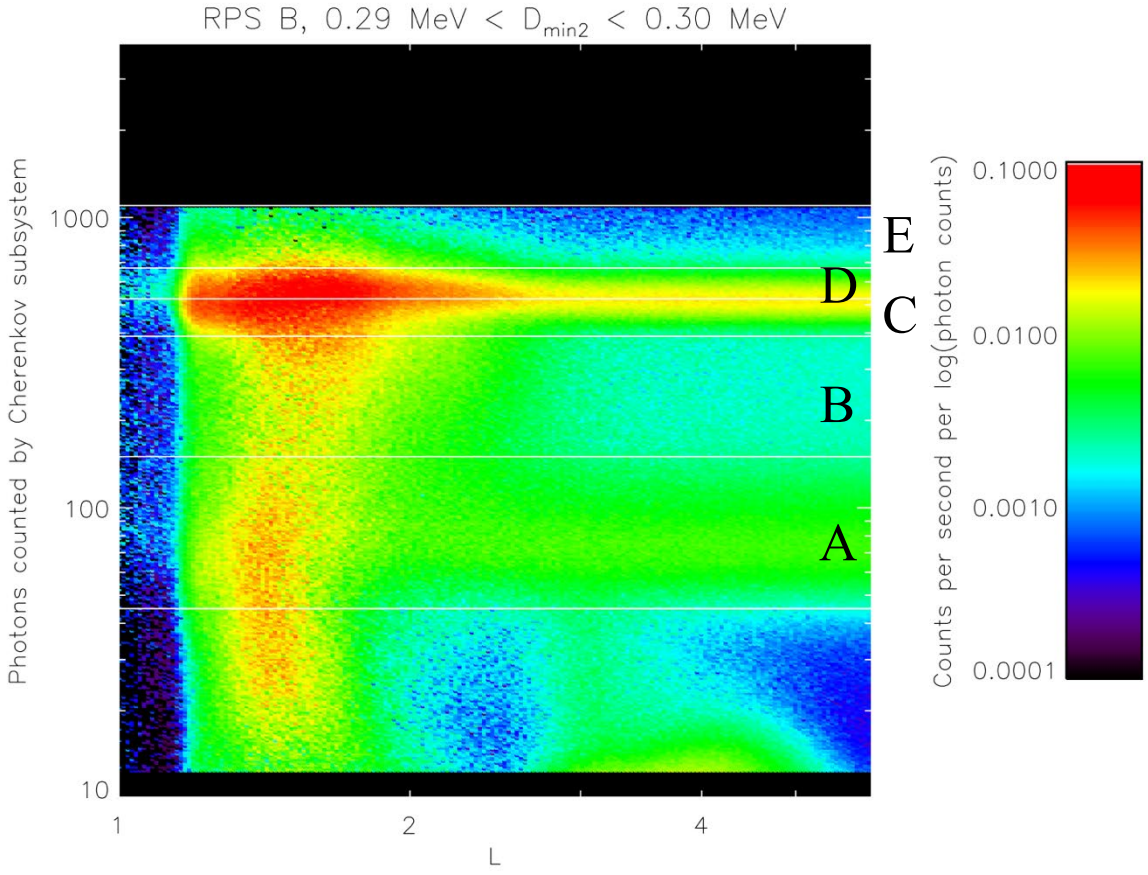

Figure 10. Variation with L of the distribution of Cherenkov photons counted by RPS B for particles with minimum-two SSDA energy deposits in the narrow range of 0.29 to 0.30 MeV. Labeled bands A-E are discussed in the main text.

Another way that this population differs from the trapped and GCR protons is in its distribution of Cherenkov light. Figure 10 shows the Cherenkov photons counted for MIP particles by RPS B as a function of L. As can be seen in Figure 7, the previous cut on minimum-two SSDA energy deposit of 0.27 to 0.33 MeV includes some of both the forward and backward "necks" for protons with energies just below that at which Cherenkov output saturates, and so for Figure 10 and for the remainder of this section we use a tighter cut of 0.29 to 0.30 MeV. The horizontal white lines in Figure 10 delimit subsets of the plot that we can compare with each other. These bands are identified by the letters A to E in the plot: A encompasses the backward proton "head," B counts events falling between the backward and forward heads, C and D divide the forward proton head about its midline, and E contains events with more photon counts than expected for a saturated forward proton signal.

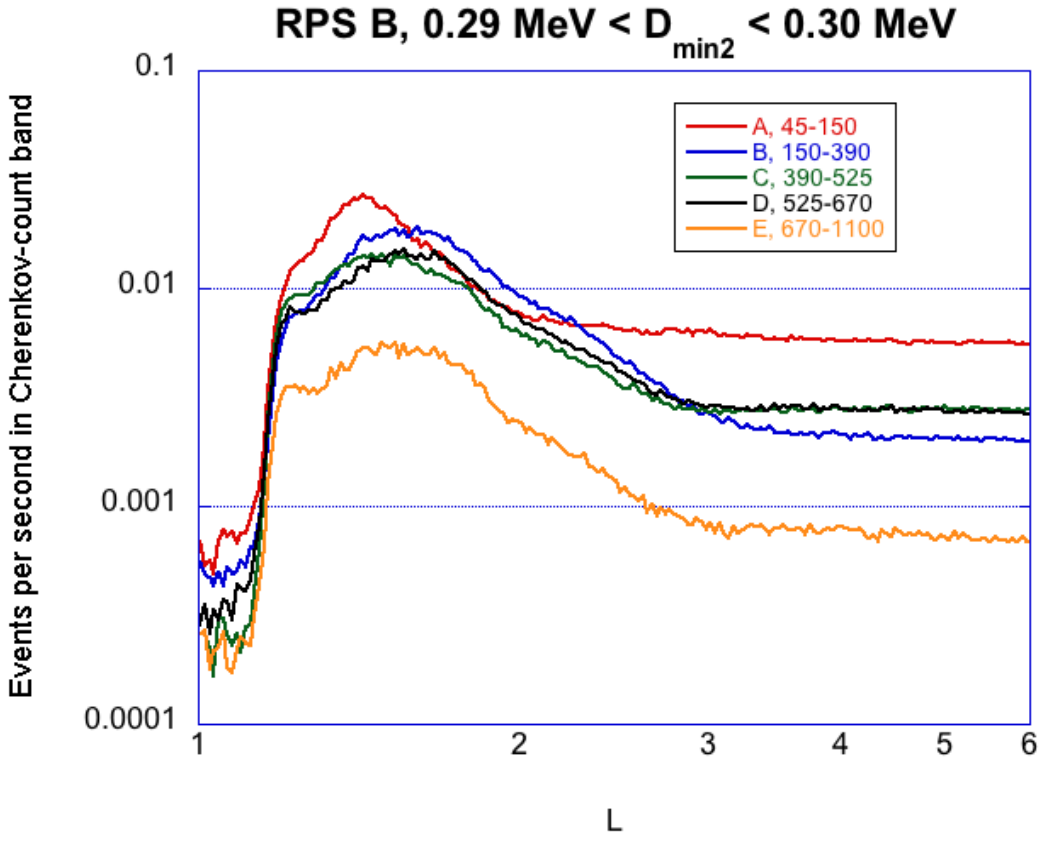

Figure 11. Countrates vs. L for events with Cherenkov photon counts falling in each of the five labeled ranges in Figure 10.

Figure 11 shows the total countrates, as a function of L, of events that have Cherenkov photon counts in the five bands in Figure 10. The boundary between ranges C and D was set so as to bisect the forward proton head, and for the GCRs at high L the two countrates are indeed essentially equal. The countrate at high L for range A is very nearly equal to the sum of the countrates in C and D, because GCR protons with energies high enough to meet the cut on minimum-two SSDA energy deposit have ranges much greater than the thickness of the sensor, so that they go through the detector stack in equal numbers in both directions. The countrate in range B, between the two proton heads, and in range E above the forward head, are substantially lower at high L than the ranges containing the forward and backward heads, as would be expected from the simulations in Figure 5.

However, the pattern starts to change when we move inward past about L = 3: the higher of the two ranges B and C splitting the forward head rises above the lower of the two, indicating a bias toward higher light output, and the supersaturated band E also begins to rise. All of these are consistent with the presence of electrons above about 30 MeV for which delta rays add to the Cherenkov light, per the simulation results shown in Figure 4e (a plot of the simulated CRA response to electrons with the tighter SSDA cut is not shown, but it is nearly identical in its distribution of events). The countrate in band B between the forward and backward heads is also enhanced, which again is consistent with the sensor's broad sub-saturated response to about 20-80 MeV electrons in Figure 4e. There is some modest enhancement in the lowest band A going inward from L = 3 to L = 2, though the baseline due to GCR protons is high. Inside L = 2 the details of the response to the inner-zone protons in each band become important, but it is clear that the response from about L = 2 to L = 3 is different from that farther out where GCR protons dominate, and as noted after Figure 9 this is too far out for trapped protons in this energy range to be present.

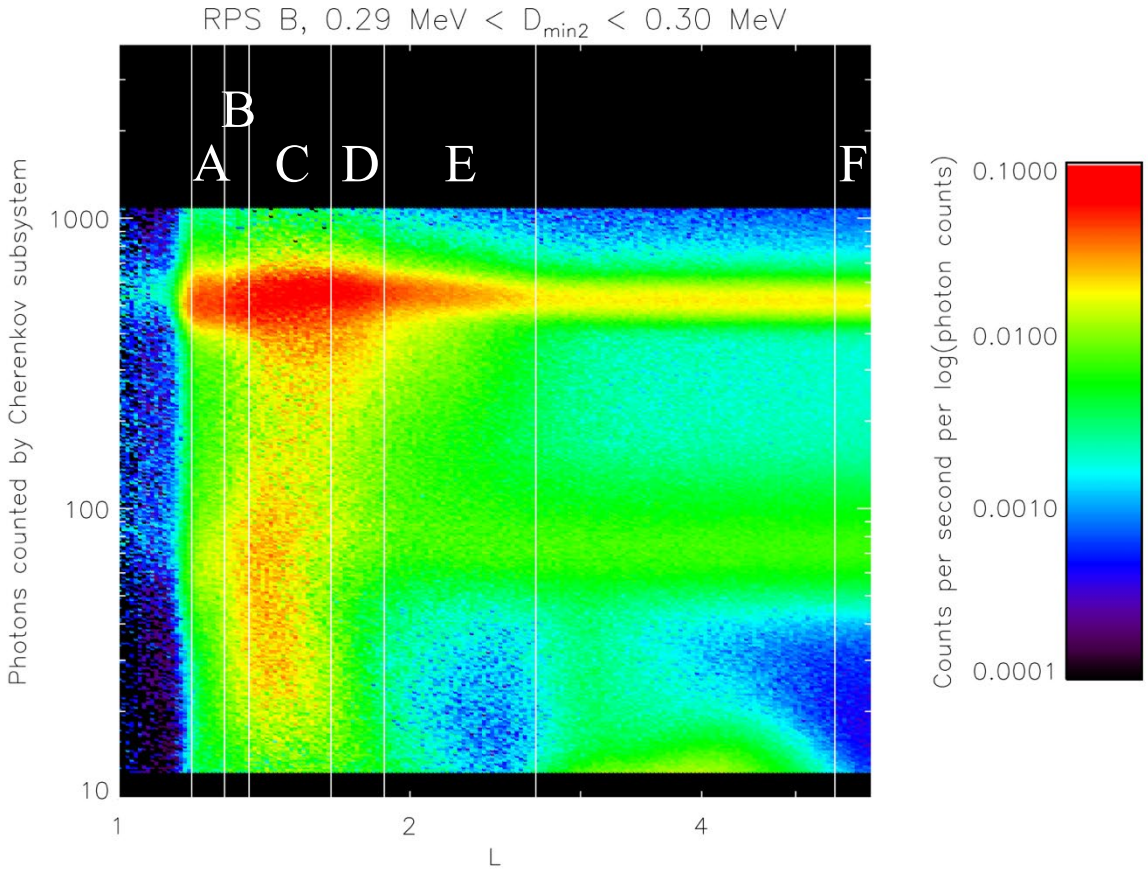

Figure 12. Variation with L of the distribution of Cherenkov photons as in Figure 10, with vertical white lines delimiting ranges of L as discussed in the main text.

Further evidence that the particle events observed in this range of L are different from the expected proton populations (or the outer-zone electrons with relatively low Cherenkov signals) is seen in the distribution of photon counts per event. Figure 12 is a duplicate of Figure 10, but with six bands labeled A-F defining ranges of L, over which we will sum these photon count distributions. Bands A-E divide up the inner zone, and band F samples the GCR flux at high L.

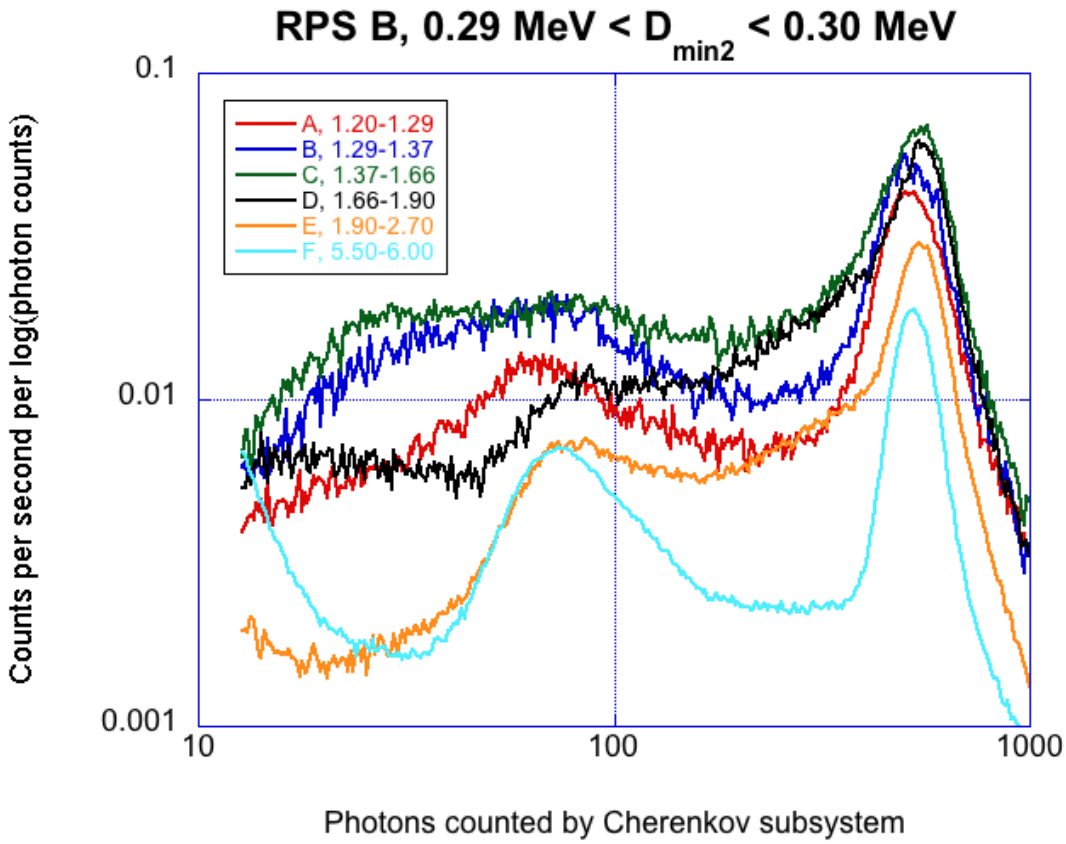

Figure 13. Distributions of Cherenkov photon counts summed over each of the L bands labeled in Figure 12.

Figure 13 shows the distributions of photons counted by the CRA averaged over all events in the six L ranges labeled A-F in Figure 12. Region F shows the cleanest sample of protons (with some residual contribution from outer-zone electrons at low photon counts); note the locations and relative heights of the two peaks corresponding to the forward and backward heads around 500 and 80 photon counts respectively, and of the region between them. Region A, deep in the inner zone (L = 1.20 to L = 1.29), likewise shows peaks for forward and backward protons, with the latter slightly lower relative to the former than is the case for region F because the trapped proton spectrum is not as hard as that of the GCR protons. The peaks in region A are also somewhat broader than in region F, but their locations are nearly the same.

The forward peak in region B is also aligned with those for A and F; however, the forward peaks for regions C, D, and E are noticeably to the right of the others' peaks. This is consistent with the presence of electrons above about 30 MeV that give a supersaturated Cherenkov signal. Moreover, while regions A-D add in a response to inner-zone protons, region E corresponds to the L range labeled E in Figure 9 which, as argued there, should be free of inner-zone protons. The contribution from GCR protons in this region can be no larger than that in region F (indeed, the two curves very nearly match up on the downslope of the backward peak below about 80 photon counts), so there must be numerous events adding to the forward peak and biasing it to higher photon counts, and also a substantial contribution just below that peak. (Region D, next inward, has a similar shape, but again there will also be some trapped protons in the mix there.) These patterns of photon counts per event are as would be expected from the simulated electron response of the sensor in Figure 4e.

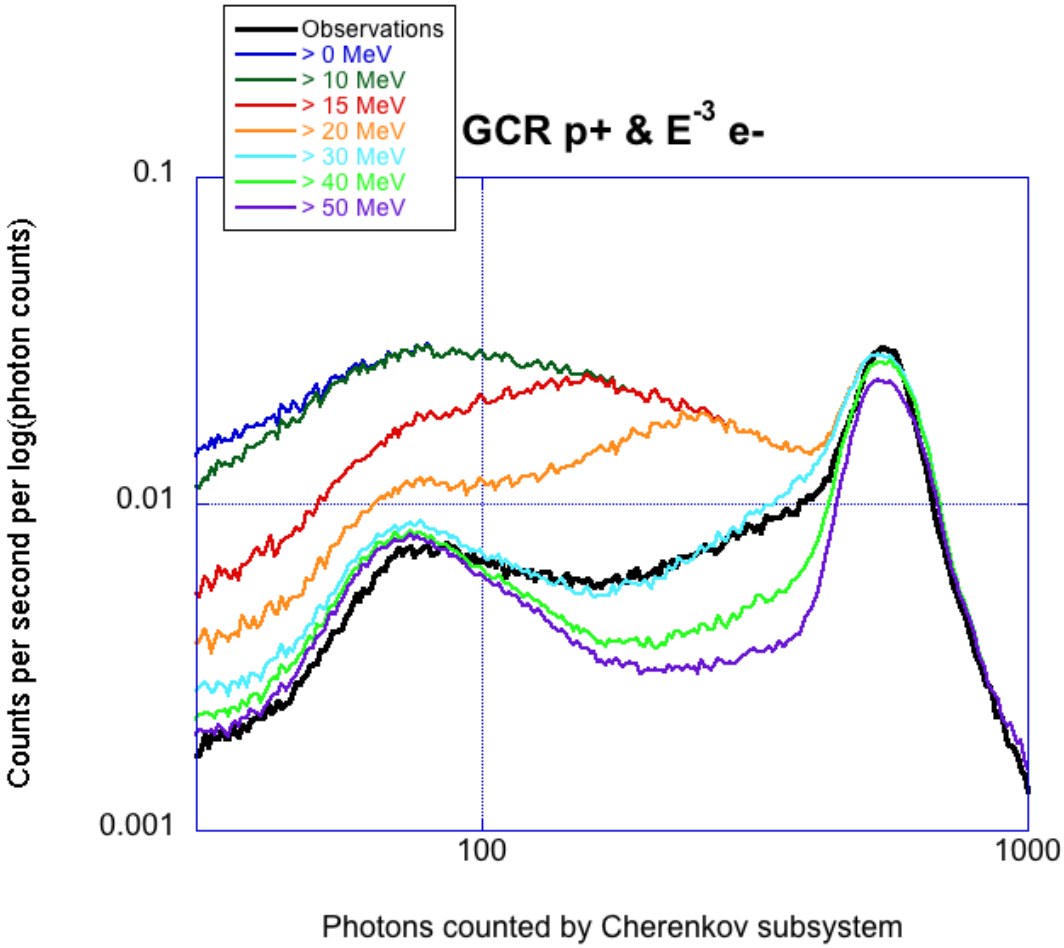

Figure 14. Distribution of Cherenkov photon counts that result from addition to the GCR protons of an electron population with E^{-3} spectrum and a lower-energy cutoff as labeled, compared with observations from region E of Figures 12 and 13.

In fact, the shape of the distribution of photon counts argues that these electrons do not merely include a subset that has energies of tens of MeV, but actually are almost completely restricted to such high energies. Figure 14 represents an attempt to reproduce the observations by convolving a set of candidate electron spectra with the response shown in Figure 4e (actually the very similar calculated response for the tighter SSDA cuts as used in Figures 10–13), and adding the resulting photon distributions to the GCR-only distribution from region F in Figure 13. The heavy black curve labeled "Observations" reproduces the curve for region E in Figure 13, for comparison. The electron spectra are proportional to E^{-3} and have lower cutoffs as labeled in the figure. The amplitude of these spectra was adjusted so these curves (except the one with the highest cutoff) matched the height of the forward peak, and even with this not-very-steep spectrum, the presence of electrons very much at all below 30 MeV gives far too many events with photon counts below this forward peak. The spectrum with a cutoff at 30 MeV gives a surprisingly good match to the observations.

As explained by Looper et al. [2], we were not able to measure the details of the generation and collection of optical photons in the CRA before flight, and thus there remain some uncertainties as to how we represented them in the model. Perhaps as a result of this, the relative amplitude of the backward peak for the curve with 30 MeV cutoff differs from the observations by about 10%, and we had to adjust the simulated counts upward by 8% to line up the forward peaks. In addition, no account has been taken of

pitch-angle distributions in any of these calculations. Nonetheless, the dramatic difference even between the photon-count distribution with a cutoff at 20 MeV and that with a cutoff at 30 MeV, which is robust against changes to the spectral slope, argues that this population consists almost entirely of electrons above about 30 MeV. We have considered various candidate sources, from Jovian electrons trapped and energized by inward diffusion to π-μ-e decays from cosmic-ray showers in the atmosphere to the survival even after twenty years of a remnant of the electrons injected by the March 1991 geomagnetic storm. Work is ongoing to evaluate these possibilities, and a refereed publication on the topic is forthcoming.

4. References

[1] Allison, J. et al., "Recent Developments in Geant4," *Nucl. Inst. and Meth. In Phys. Res. A*, **835**, 186-225, doi: 10.1016/j.nima.2016.06.125. 2016.

[2] Looper, M. D.; T. P. O'Brien; and J. E. Mazur, *Relativistic Proton Spectrometer Detector Calibration*, Aerospace Report Number ATR-2021-02025, The Aerospace Corporation, El Segundo, CA. 2021.

[3] Mazur, J. E.; A. Lin; D. Mabry; N. Katz; Y. Dotan; J. George; J. B. Blake; M. Looper; M. Redding; T. P. O'Brien; J. Cha; A. Birkitt; P. Carranza; M. Lalic; F. Fuentes; R. Galvan; and M. McNab, "The Relativistic Proton Spectrometer (RPS) for the Radiation Belt Storm Probes Mission," *Space Sci. Rev*. **179** (1-4), 221-261, doi: 10.1007/s11214-012-9926-9. 2013.

[4] O'Brien, T. P.; M. D. Looper; J. E. Mazur; and E. L. Mazur (2021), *Relativistic Proton Spectrometer Flux Determination and Data Products*, Aerospace Reporrt Number ATR-2021-02018, The Aerospace Corporation, El Segundo, CA. 2021.

AEROSPACE REPORT NO.
ATR-2021-02026

Relativistic Proton Spectrometer Electron Response

Cognizant Program Manager Approval:

Robert D. Rutledge, DIRECTOR - DEPARTMENT
SPACE SCIENCE APPLICATIONS LABORATORY
PHYSICAL SCIENCES LABORATORIES
ENGINEERING & TECHNOLOGY GROUP

Aerospace Corporate Officer Approval:

Todd M. Nygren, SENIOR VP ENGINEERING & TECHNOLOGY
OFFICE OF EVP

Content Concurrence Provided Electronically by:

Mark D. Looper, RESEARCH SCIENTIST
MAGNETOSPHERIC & HELIOSPHERIC SCIENCES
SPACE SCIENCES DEPARTMENT
ENGINEERING & TECHNOLOGY GROUP

Office of General Counsel Approval Granted Electronically by:

Kien T. Le, ASSISTANT GENERAL COUNSEL
OFFICE OF THE GENERAL COUNSEL
OFFICE OF GENERAL COUNSEL & SECRETARY

SY0876

AEROSPACE REPORT NO.
ATR-2021-02026

Relativistic Proton Spectrometer Electron Response

Export Control Office Approval Granted Electronically by:

Angela M. Farmer, SECURITY SUPERVISOR
GOVERNMENT SECURITY
SECURITY OPERATIONS
OFFICE OF THE CHIEF INFORMATION OFFICER

SY0876